RESEARCH ARTICLE

ADVANCED MATERIALS INTERFACES
Open Access

www.advmatinterfaces.de

Digital Etching of Molybdenum Interconnects Using Plasma Oxidation

*Ivan Erofeev, Antony Winata Hartanto, Muhaimin Mareum Khan, Kerong Deng, Krishna Kumar, Zainul Aabdin, Weng Weei Tjiu, Mingsheng Zhang, Antoine Pacco, Harold Philipsen, Angshuman Ray Chowdhuri, Han Vinh Huynh, Frank Holsteyns, and Utkur Mirsaidov**

Molybdenum (Mo) has a high potential of becoming the material of choice for sub-10 nm scale metal structures in future integrated circuits (ICs). Manufacturing at this scale requires exceptional precision and consistency, so many metal processing techniques must be reconsidered. In particular, present direct wet chemical etching methods produce anisotropic etching profiles with significant surface roughness, which can be detrimental to device performance. Here, it is shown that polycrystalline Mo nanowires can be etched uniformly using a cyclic two-step "digital" method: the metal surface is first oxidized with isotropic oxygen plasma to form a layer of MoO_3, which is then selectively removed using either wet chemical or dry isotropic plasma etching. These two steps are repeated in cycles until the intended metal recess is achieved. High uniformity of plasma oxidation defines the etching uniformity, and small metal recess per cycle (typically 1–2 nm) provides precise control over the etching depth. This method can replace wet etching where high etching precision is needed, enabling the reliable manufacturing of nanoscale metal interconnects.

1. Introduction

Integrated circuits (ICs) have been steadily scaling down over the past few decades,[1,2] driven by the ever-growing demand for higher computational power and efficiency. The resulting rapid increase in the spatial density of IC elements, such as transistors, has led to the respective shrinking in the dimensions of metal interconnects,[3,4] with the smallest of them currently being only ≈10 nm in width. Most interconnects are made of copper (Cu) as it offers the best combination of high conductivity and low cost,[5,6] however, Cu shows a significant increase in resistivity at wire dimensions below its electron mean free path length of 40 nm (at 20 °C).[7–11] Therefore, alternative materials have been proposed for the thinnest interconnects which surpass Cu at the critical dimension (CD) of 10 nm and below. Among them, molybdenum (Mo) is the first candidate.[12–16] Despite its higher bulk resistivity value, the electron mean free path length of only 11.2 nm[11] ensures much better scalability of Mo wires and enables better performance at CDs below 10 nm when compared to Cu. At the same time, Mo is a new material for semiconductor manufacturing, which brings new processing challenges, especially given the very high precision required for

I. Erofeev, A. W. Hartanto, M. M. Khan, K. Deng, K. Kumar, U. Mirsaidov
Centre for BioImaging Sciences
Department of Biological Sciences
National University of Singapore
Singapore 117557, Singapore
E-mail: mirsaidov@nus.edu.sg

I. Erofeev, A. W. Hartanto, M. M. Khan, K. Deng, U. Mirsaidov
Centre for Advanced 2D Materials and Graphene Research Center
National University of Singapore
Singapore 117546, Singapore

Z. Aabdin, W. W. Tjiu, M. Zhang
Institute of Materials Research and Engineering
Agency for Science
Technology and Research (A*STAR)
Singapore 138634, Singapore

A. Pacco, H. Philipsen, F. Holsteyns
imec
Kapeldreef 75, Leuven B-3001, Belgium

A. R. Chowdhuri, H. V. Huynh
Department of Chemistry
National University of Singapore
Singapore 117543, Singapore

U. Mirsaidov
Department of Physics
National University of Singapore
Singapore 117551, Singapore

U. Mirsaidov
Department of Materials Science and Engineering
National University of Singapore
Singapore 117575, Singapore

The ORCID identification number(s) for the author(s) of this article can be found under https://doi.org/10.1002/admi.202400558

© 2024 The Author(s). Advanced Materials Interfaces published by Wiley-VCH GmbH. This is an open access article under the terms of the Creative Commons Attribution License, which permits use, distribution and reproduction in any medium, provided the original work is properly cited.

DOI: 10.1002/admi.202400558

ADVANCED MATERIALS INTERFACES Open Access
www.advmatinterfaces.de

interconnects with CD of 10 nm and below.[17–19] For instance, a reliable method for highly uniform isotropic etching (i.e., same etch rate in all directions, as opposed to highly anisotropic reactive ion etching), critical for the manufacturing of complex 3D structures such as 3D flash memory stacks or backside power delivery network,[14,20–22] has not been established yet. Conventional direct wet chemical etching faces anisotropy issues related to the nanocrystallinity of metal structures, which cause increasingly non-uniform etching profiles.[18] Such non-uniformities can cause severe loss of performance and device failures and are unacceptable in a mature manufacturing process.

This issue can be overcome by introducing a cyclic two-step etching approach,[23] where a surface layer of the polycrystalline metal is first converted into an amorphous material such as metal oxide, and then this layer is selectively etched at the second step. It is important to note that the amorphous layer must be easily etchable so that no insoluble subproducts remain on the surface. For relatively small metal recess per cycle and high etching control, such methods are usually referred to as atomic layer etching (ALE). This approach is also called “digital etching” due to the discreet amount of metal recess over multiple cycles. The formation of an amorphous Mo oxide layer has been demonstrated using high-temperature ozone, and the oxide layer was then dissolved in an ammonia (NH_4OH) aqueous solution.[24–26] Other examples include the use of oxygen plasma for Mo oxidation and chlorine plasma for selective oxide etching,[27] or a combination of fluorine and argon plasmas.[28] However, both plasma methods have only been tested on Mo blanket thin films, for which it is hard to distinguish between isotropic and anisotropic etching behavior. Our previous work focused on isotropic digital etching of patterned Mo nanowires (NWs) using wet chemical solutions for both oxidation and etching steps, where we demonstrated the formation of a stable and uniform MoO_3 layer by reducing the solution temperature.[29] While this approach yielded smooth etch profiles that are superior to the etch profiles obtained by direct etching, it still had a limitation. Namely, we noted a gradual increase in the large-scale surface roughness (referred to as waviness) over multiple cycles. We attributed the increase in waviness to the slow oxidation rate, which makes the oxidation facet-dependent, similar to the direct etching approach. Hence, a great recess control and a smooth metal surface did not translate into a significant improvement in the overall etch uniformity.

According to the Cabrera-Mott theory of metal oxidation,[30–32] using plasma oxidation in the first step of a digital etching cycle has several advantages when compared to wet or hot gas oxidation. Plasma oxidation should lead to a faster surface oxidation, as atomic oxygen species induce a stronger Mott potential across the oxide layer.[33] This also makes oxidation more controllable than with high-temperature gas oxidation, as thermal diffusion of metal ions through the oxide is negligible at room temperature.[32]

In this study, we establish a two-step digital etching process for patterned Mo NWs where surface oxidation by oxygen plasma, the first step, is followed by either wet or dry selective etching of the oxide, the second step. In this process, the oxide thickness and the metal recess can be easily controlled with the oxygen plasma power, where the plasma oxidizes Mo to its maximum oxidation state Mo^{6+}, making the oxide layer fully soluble even in de-ionized (DI) water. Moreover, we show that if the oxidation time is within the optimal range of 1–2 min, the metal recess stays uniform over many cycles.

2. Results and Discussion

The schematic of a TEM (transmission electron microscope) chip with patterned Mo NWs in the process of TEM imaging is shown in **Figure 1A**. The two-step “digital” etching method with plasma oxidation and selective etching of the oxide layer is schematically shown in Figure 1B. We first focus on the oxidation control because it is the oxidation step that defines the quality and rate of etching. As a uniform metal recess is required in many applications, e.g., when etching vertical stacks of nanostructures, we ensured the plasma in our experiments was isotropic, i.e., no bias was applied to the NW samples. We used an oxygen–nitrogen (1:3) gas mixture at a pressure of 120 mTorr (similar to industrially used parameters) to create a plasma with an ICP (inductively coupled plasma) power of 25 or 75 W. Samples were placed downstream (toward the vacuum pump) perpendicular to the plasma flow to maximize the plasma–surface interaction. We imaged Mo NWs with TEM before and after the exposure to determine the oxide thickness and metal recess depth through automated image analysis based on edge detection algorithms. Example TEM images of NWs before and after oxidation are shown in Figure 1C. Figure 1D presents the oxide thickness measurements after 30 s to 10 min of plasma exposure: the oxide growth rate slows down steadily, and the oxide thickness at 75 W is about twice that produced at 25 W. More TEM images of oxidized Mo NWs are shown in Figure S1 (Supporting Information). The metal recess follows the same trend, as shown in Figure 1E, with the observed ratio of metal oxide to the consumed metal being about three. Given the Mo lattice parameter $a = 3.15$ Å, this means that each nanometer of the oxide consumes about one atomic layer of Mo. The root-mean-square error (RMSE) value of the edge profiles measured after four cycles depends very weakly on the oxidation time. Note that the metal recess scan for multiple cycles has been only done for the higher power of 75 W, as it offered a larger variability and a higher recess rate overall.

To learn more about the surface layer, we first analyzed the electron diffraction pattern of oxidized NWs. As seen in **Figure 2A**, the diffraction pattern only shows rings of spots specific to polycrystalline metallic Mo, in particular those corresponding to spacings between {110}, {200}, and {211} Mo planes. This means that the surface layer shows no crystalline structure, i.e., it is amorphous, as also confirmed by high-resolution TEM images (Figure S2, Supporting Information). The FIB (focused ion beam) cross-section STEM (scanning TEM) image and electron energy loss spectroscopy (EELS) maps and line profiles shown in Figure 2B display uniform oxide coverage of the Mo NWs from both sides and the top, confirming the isotropic oxidation. The EELS spectrum from the surface layer only shows Mo and O signals, which suggests pure Mo oxide. Note that the underlying SiO_2 layer is partly etched down between the Mo NWs as a result of HF (hydrofluoric acid) treatment during the fabrication of the chips. Figure 2C shows X-ray photoelectron spectroscopy (XPS) signals of Mo thin film samples before oxidation, after oxidation with oxygen–nitrogen plasma, and after oxide dissolution in 1 M aqueous HCl solution, in the range of binding energy typical for Mo 3d electrons.[15,34] The initial clean sample

© 2024 The Author(s). Advanced Materials Interfaces published by Wiley-VCH GmbH
21967350, 2025, 1, Downloaded from https://advanced.onlinelibrary.wiley.com/doi/10.1002/admi.202400558, Wiley Online Library on [06/05/2025]. See the Terms and Conditions (https://onlinelibrary.wiley.com/terms-and-conditions) on Wiley Online Library for rules of use; OA articles are governed by the applicable Creative Commons License

21967350, 2025, 1, Downloaded from https://advanced.onlinelibrary.wiley.com/doi/10.1002/admi.202400558, Wiley Online Library on [06/05/2025]. See the Terms and Conditions (https://onlinelibrary.wiley.com/terms-and-conditions) on Wiley Online Library for rules of use; OA articles are governed by the applicable Creative Commons License

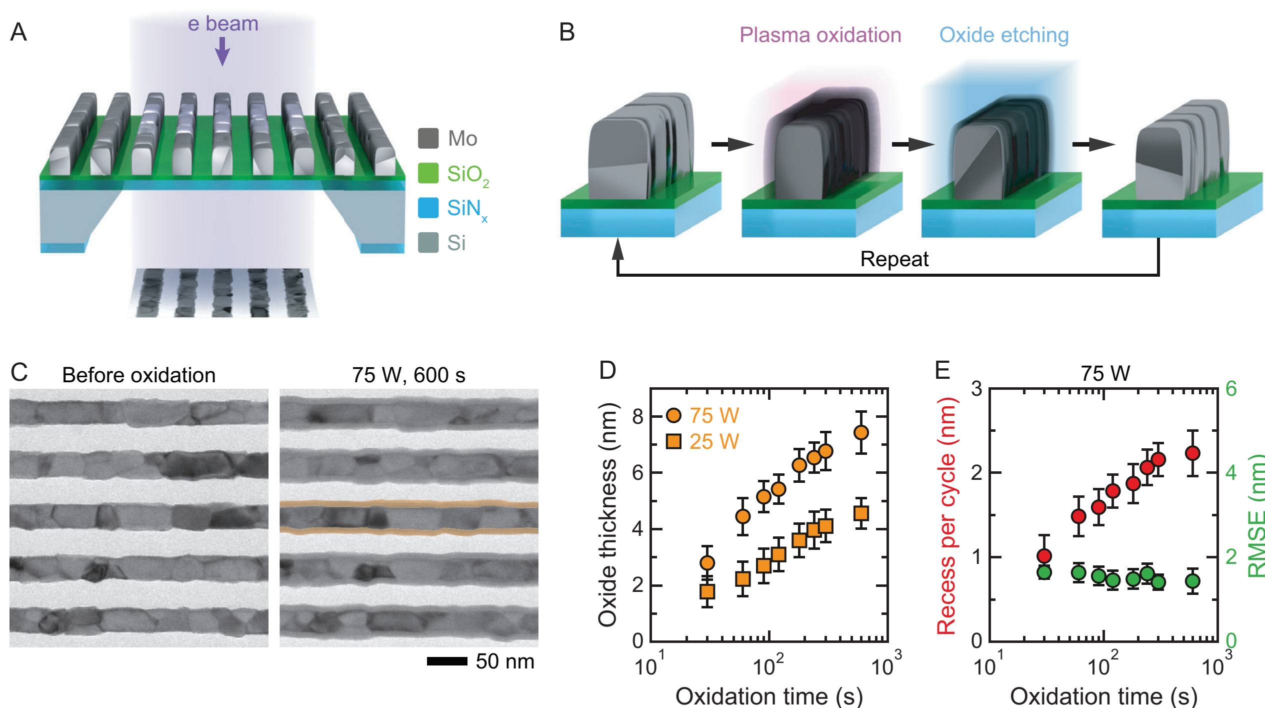

Figure 1. Overview of digital etching and oxidation control. A) Schematic of patterned Mo NWs on a free-standing SiO_2/SiN_x as imaged with TEM. B) Schematic of the two-step "digital" etching process with plasma oxidation and selective oxide etching. C) TEM images of NWs before and after oxidation at 75 W for 600 s. D) Thickness of plasma-induced Mo oxide layer as a function of the plasma exposure time with 25 and 75 W of ICP power. E) Mean metal recess per cycle and edge roughness after four cycles characterized by the RMSE value of the edge profile as functions of the plasma exposure time with 75 W of ICP power.

shows only the metallic Mo^0 doublet, while the spectrum of the oxidized Mo film is a combination of Mo^0 and Mo^{6+}. This indicates that the surface Mo is fully oxidized by the oxygen plasma, and the oxide layer consists exclusively of MoO_3 species. At the same time, the oxide layer thickness is smaller than the X-ray penetration depth, which explains the presence of Mo^0 signal from the oxidized film. After the oxide layer dissolution, the spectrum again only features Mo^0 signal. The very minor contributions from Mo^{4+} and Mo^{6+} in the films before oxidation and after oxide dissolution are due to unavoidable exposure of the samples to air. Note that Mo^0 peaks show significant asymmetry due to high metal conductivity, while Mo^{6+} peaks are symmetric.[35]

To visualize the oxide layer dissolution, we performed in situ TEM studies with a solution flowing through the liquid cell (**Figure 3A**), where two SiN_x membranes isolate the reaction area from the vacuum of the electron microscope. Figure 3B displays a series of TEM images of the oxide layer dissolution in a liquid cell with a flow of 1 M aqueous solution of NH_4OH. Figure 3C presents the quantification of oxide dissolution by measuring the averaged relative contrast dip near the metal surface over time, which shows the local thickness of the amorphous oxide layer along the line of sight. The dissolution process only takes ≈2 s, and the dissolution front can be seen to move both toward the metal surface and the substrate, according to Figure 3C. If DI water is used for MoO_3 dissolution, the remaining metal surface is equally clean, although the dissolution takes considerably longer, ≈2 min (Figure 3D,E). It should be noted that while NH_4OH offers a much faster dissolution rate of MoO_3 than DI water, its selectivity toward metallic Mo is moderate, even at room temperature (Figure S3, Supporting Information). When the oxidized Mo NWs were kept inside the 1 M NH_4OH solution for 10 min, we observed a notable etching of metal past the metal–oxide interface. After some testing of alternative solutions, we decided to use a 1 M aqueous solution of HCl for the oxide dissolution step in the following experiments, as it provided the same fast dissolution and a much better selectivity.

Clean, fast, and highly selective dissolution of the MoO_3 surface layer allows for the cyclic "digital etching" approach when the oxidation and oxide dissolution steps are repeated multiple times to achieve the desired metal recess. Based on the parameter scan shown in Figure 1D,E, we selected the higher oxidation power of 75 W and the oxidation time of 2 min, as this combination shows the optimal trade-off between the recess amount and the oxidation time. TEM images of the same area of a sample every two cycles, for a total of eight cycles, are shown in **Figure 4A** (Video 3, Supporting Information), while Figure 4B presents the superimposed outlines of Mo NWs in the same area, showing a gradual and uniform recess. Figure 4C plots the mean metal recess over the eight cycles, demonstrating a highly stable etching behavior with a mean recess rate of 1.7 nm/cycle. Figure 4D shows that surface uniformity stays at the same levels, both at the atomic scale and the grain scale (defined as roughness and waviness, respectively; see Experimental Section). The commonly used RMSE of the edge profile stays below 1.5 nm through the entire etching process, indicating a highly uniform etching process.

© 2024 The Author(s). Advanced Materials Interfaces published by Wiley-VCH GmbH

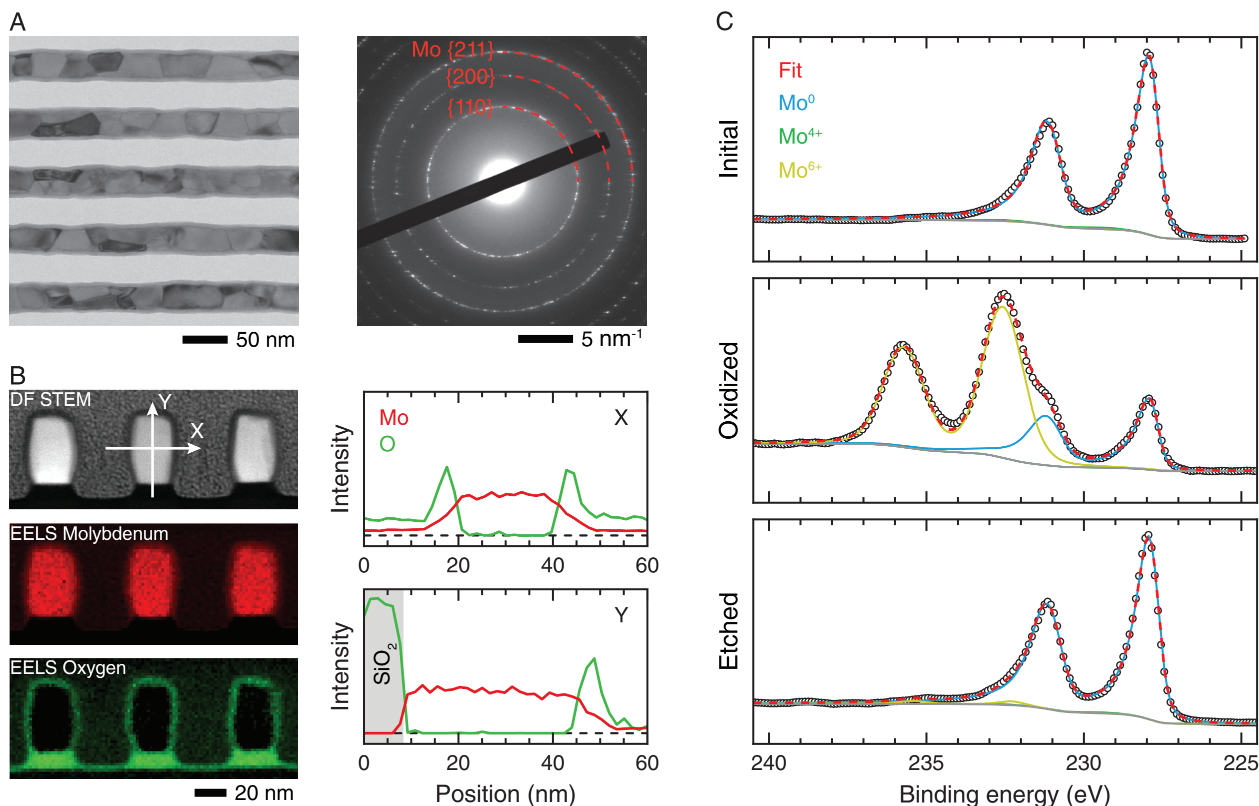

Figure 2. Mo oxide characterization. A) TEM (left) and electron diffraction (right) images of oxidized Mo NWs. B) Cross-section bright-field STEM image and EELS elemental maps for Mo and O elements of oxidized Mo NWs, as well as EELS line profiles across a single Mo NW (along X and Y lines in the STEM image). C) XPS spectra in the range of $Mo3d_{5/2}$ and $Mo3d_{3/2}$ peaks for Mo films before oxidation, after oxidation, and after selective etching of Mo oxide measured at the take-off angle of 90°. The grey curves show the background level.

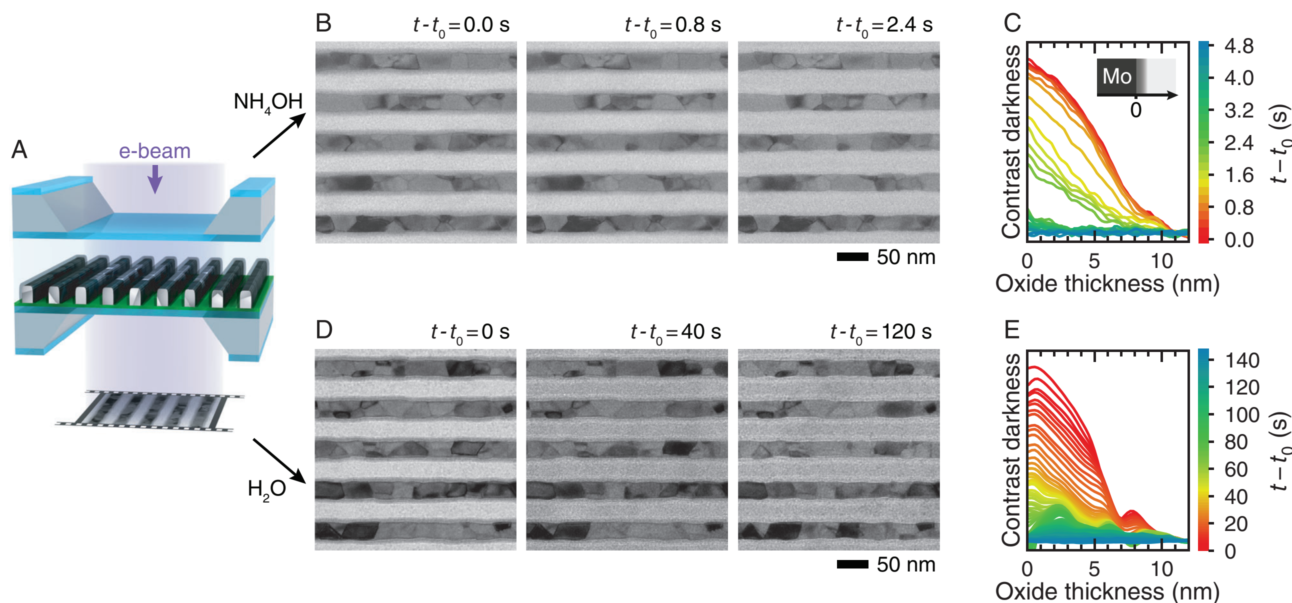

Figure 3. In situ Mo oxide dissolution. A) Schematic of a TEM liquid cell with Mo NWs used for in situ TEM imaging. B) In situ TEM image series showing the dissolution of MoO_3 surface layer in the flow of 1 M aqueous NH_4OH solution (Video 1, Supporting Information). C) Oxide layer dissolution quantified by the change in TEM image contrast next to the Mo metal surface (at 0 nm mark): initial dark contrast area gradually becomes brighter and thinner, reflecting the direction and rate of the MoO_3 layer dissolution. D) In situ TEM image series showing the dissolution of MoO_3 surface layer in the flow of DI water (Video 2, Supporting Information). E) Similar plots as in (C), for the case of MoO_3 dissolution in DI water.

© 2024 The Author(s). Advanced Materials Interfaces published by Wiley-VCH GmbH

21967350, 2025, 1, Downloaded from https://advanced.onlinelibrary.wiley.com/doi/10.1002/admi.202400558, Wiley Online Library on [06/05/2025]. See the Terms and Conditions (https://onlinelibrary.wiley.com/terms-and-conditions) on Wiley Online Library for rules of use; OA articles are governed by the applicable Creative Commons License

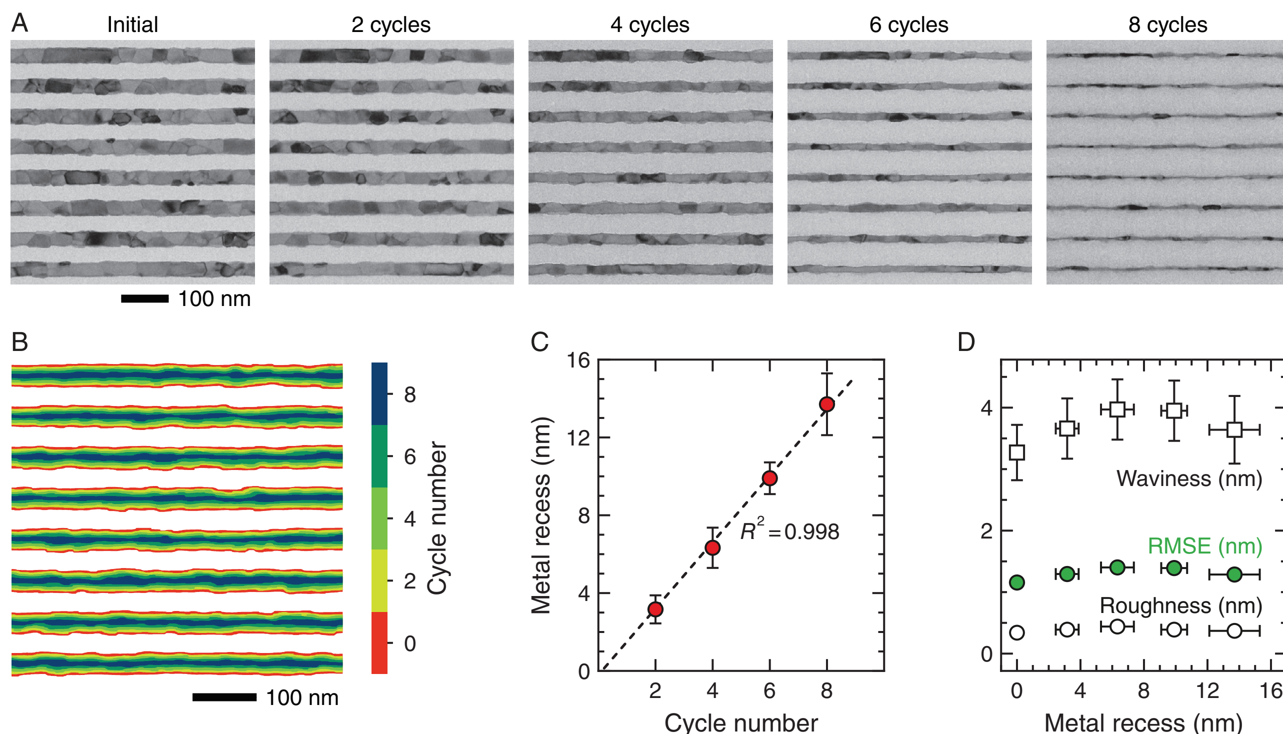

Figure 4. Cyclic digital etching with plasma oxidation at 75 W of ICP power. A) TEM images of the same NWs after every two digital etching cycles, with the ICP power and oxidation time set to 75 W and 1 min, respectively. After eight cycles, the mean thickness of the NWs is reduced from 33 nm to 6 nm. B) Outlines of the same NWs over eight etching cycles. The initial state is marked as "0 cycle". C) Metal recess over eight etching cycles. D) Plots of NW edge waviness, roughness, and RMSE characterizing the etching uniformity over eight etching cycles.

The cyclic process presented above involves both dry and wet steps, which might not be the preferred scheme for industrial applications, as it requires a drying step after each cycle. This not only increases the process complexity and duration but also can lead to the collapse of fine, tall nanostructures due to capillary forces. To avoid this issue, selective oxide etching can be performed with a dry method, e.g., using plasma etching with a combination of gases containing hydrogen and chlorine.[27] We used a conventional reactive ion etching setup to test this approach for the etching of Mo NWs. **Figure** 5A shows the schematic of this process with cycled O_2 and Cl_2 plasmas. Figure 5B presents TEM images of Mo NWs before the processing, after 2 min of O_2 plasma oxidation, and after 2 min of Cl_2 plasma etching. Here, we ran the plasma discharges without bias to ensure isotropic oxidation and oxide etching. Note that while a higher temperature helps to improve oxidation,[26] etching selectivity of Cl_2 plasma toward Mo metal reduces dramatically above 40 °C.[27] Therefore, we increased the substrate temperature to 50 °C for the oxidation step and decreased it to 0 °C for the etching step. As a result, the clean and smooth metal surface after the etching of Mo oxide with a Cl_2 plasma is similar to that after the oxide dissolution using wet chemical solutions.

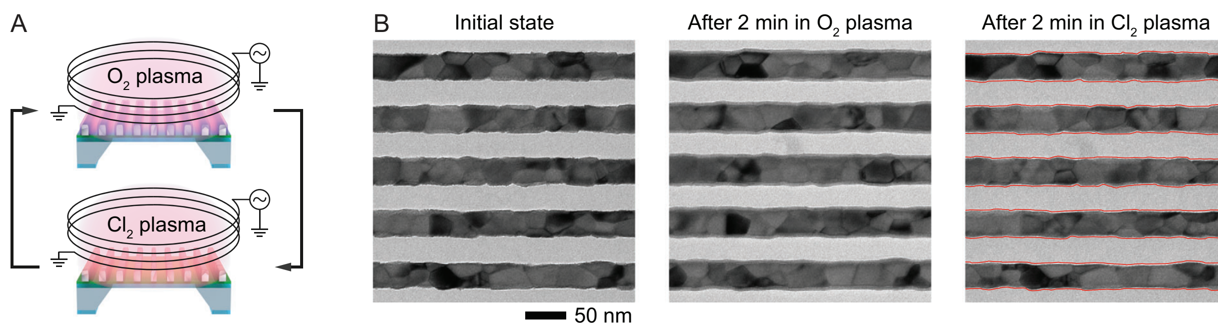

Figure 5. Fully dry Mo etching cycle. A) Schematic of Mo oxidation with O_2 plasma and Mo oxide etching with Cl_2 plasma using the same plasma setup. B) TEM images of the same Mo NWs before the processing, after plasma oxidation, and after selective plasma etching of the oxide layer. Red outlines in the right image panel mark the NW edges before the processing.

© 2024 The Author(s). Advanced Materials Interfaces published by Wiley-VCH GmbH

21967350, 2025, 1, Downloaded from https://advanced.onlinelibrary.wiley.com/doi/10.1002/admi.202400558, Wiley Online Library on [06/05/2025]. See the Terms and Conditions (https://onlinelibrary.wiley.com/terms-and-conditions) on Wiley Online Library for rules of use; OA articles are governed by the applicable Creative Commons License

3. Conclusions

We have studied cyclic two-step digital etching of Mo NWs for interconnect applications using plasma oxidation. We have shown that the surface oxide after O_2 plasma treatment is amorphous MoO_3, which can be fully dissolved using a range of wet chemical solutions, including DI water, or etched selectively using a Cl_2 plasma. In our cyclic experiment, the etching rate and uniformity remained consistent over multiple oxidation–dissolution cycles, offering a high level of etching control and precision. We stress that the plasma parameters, such as power and pressure, largely depend on the particular setup and can be easily optimized for different setups. The density of atomic oxygen species plays an important role, so optimizing plasma composition and pressure, as well as sample position and orientation, can vastly increase the oxidation efficiency.

4. Experimental Section

Experimental Procedures: The process for fabricating the chips with patterned Mo NWs was described in detail in our previous study.[29] Plasma oxidation of these Mo NWs was done using PIE Scientific Tergeo-EM (PIE Scientific LLC, Union City, CA, USA) with the ICP power set to 25 or 75 W (the highest available). The plasma (25% O_2 and 75% N_2) was generated in the remote mode, and the NW samples were placed downstream perpendicular to the flow, such that the plasma spread uniformly over the sample surface. Oxide dissolution was performed in DI water, the aqueous solutions of HCl (1M, pH ≈ 0), or NH_4OH (1M, pH ≈ 11.6). Oxford Instruments PlasmaPro 100 Cobra (Oxford Instruments Plasma Technology, Yatton, Bristol, UK) was used to run a fully dry etching process. Ar was used in both O_2 and Cl_2 discharges with 75% of the total gas flow, and 100% Ar was used for purging the chamber between the steps.

Characterization: Routine TEM images were obtained with a JEOL 2010F electron microscope (JEOL Ltd., Tokyo, Japan) equipped with a Gatan OneView camera (Gatan Inc., Pleasanton, CA, USA) at 200 kV and using a Thermo Fisher Titan S/TEM (Thermo Fisher Scientific Ltd., Hillsboro, OR, USA) equipped with a Gatan K2 IS camera at 300 kV. EELS data were recorded using a Thermo Fisher Tecnai G2 TF20 S/TEM equipped with a Fischione Model 3000 annular dark field (ADF) STEM detector (E.A. Fischione Instruments Inc., Export, PA, USA) and a Gatan GIF Quantum Model 963 EELS detector at 200 kV. In situ TEM studies were conducted using our custom flow holder, with a solution flowing into a flow cell at a rate of 2µL min^{-1}.[36,37] In situ movies were recorded with the JEOL 2010F TEM at a frame rate of five frames per second and the electron flux of 10 e A^{-2} s^{-1}. The XPS studies were conducted using a Kratos Amicus/ESCA 3400 spectrometer (Kratos Analytical Ltd., Manchester, UK) at 0.1 eV resolution with 1 s dwell time. XPS fitting was performed using AAnalyzer software package.[38]

Image Processing: A series of image processing algorithms were developed using Python,[39] for frame alignment, image rotation, edge detection, and measurement of areas of connected regions. To quantify the metal oxide thickness and metal recess in Figures 1D,E and 4C,D, the same area of the NW sample was imaged before oxidation, after oxidation, and after the oxide dissolution. The images were aligned, and each edge profile was detected. Oxide thickness was then calculated as the mean difference between the profiles of the final and the oxidized samples, and the metal recess was the mean difference between the profiles of the final and the initial samples. For each data point, a square TEM image was analyzed with ten NWs (i.e., 640 nm by 640 nm, with a total metal edge length of 12.8 µm). Error bars at each data point represent one standard deviation σ. For the quantification of oxide layer dissolution in Figure 3C, E, the pixel brightness level was measured next to the detected edges and then summed up along each edge and for all edges. Finally, the local background level was subtracted, and the resulting value was inverted. The analysis of edge variance, as presented in Figure 4D, was performed as follows: Using low- and high-pass filters in Fourier space, each edge profile was decomposed into two components: one with features below 1 nm representing atomic-scale roughness and one with features above that, outlining larger non-uniformities such as grain facets. Importantly, these two profiles sum up to the original edge profile. Then a standard deviation σ was computed for each part, and 3σ of the small-scale and large-scale profiles was called "roughness" and "waviness," respectively. The sum of these two values equals the standard line-edge roughness (LER) value. The RMSE value was calculated according to its definition.[40]

Supporting Information

Supporting Information is available from the Wiley Online Library or from the author.

Acknowledgements

This work was supported by the Singapore National Research Foundation's Competitive Research Program funding (NRF-CRP23-2019-0001).

Conflict of Interest

The authors declare no conflict of interest.

Data Availability Statement

The data that support the findings of this study are available from the corresponding author upon reasonable request.

Keywords

atomic layer etching (ALE), integrated circuits (ICs), interconnects, metal etching, plasma oxidation

Received: June 26, 2024
Revised: October 16, 2024
Published online: November 12, 2024

[1] A. Razavieh, P. Zeitzoff, E. J. Nowak, *IEEE Trans. Nanotechnol.* **2019**, *18*, 999.
[2] A. Spessot, B. Parvais, A. Rawat, K. Miyaguchi, P. Weckx, D. Jang, J. Ryckaert, 2020 IEEE BiCMOS and Compound Semiconductor Integrated Circuits and Technology Symp. (BCICTS) **2020**, 1, https://doi.org/10.1109/BCICTS48439.9392980.
[3] D. Gall, 2018 IEEE Int. Interconnect Technology Conf. (IITC) **2018**, 157. https://doi.org/10.1109/IITC.8456810.
[4] D. Gall, 2020 International Symposium on VLSI Technology, Systems and Applications (VLSI-TSA) 112. https://doi.org/10.1109/VLSI-TSA48913.2020.9203700.
[5] R.-H. Kim, B. H. Kim, T. Matsuda, J. N. Kim, J. M. Baek, J. J. Lee, J. O. Cha, J. H. Hwang, S. Y. Yoo, K.-M. Chung, K. H. Park, J. K. Choi, E. B. Lee, S. D. Nam, Y. W. Cho, H. J. Choi, J. S. Kim, S. Y. Jung, D. H. Lee, I. S. Kim, D. W. Park, H. B. Lee, S. H. Ahn, S. H. Park, M.-C. Kim, B. U. Yoon, S. S. Paak, N.-I. Lee, J.-H. Ku, J. S. Yoon, H.-K. Kang, E. S. Jung, Eds., *2014 IEEE International Electron Devices Meeting* 32.32.31-32.32.34, **2014**, 7047153, https://doi.org/10.1109/IEDM.
[6] A. Pyzyna, R. Bruce, M. Lofaro, H. Tsai, C. Witt, L. Gignac, M. Brink, M. Guillorn, G. Fritz, H. Miyazoe, D. Klaus, E. Joseph, K. P. Rodbell, C. Lavoie, D.-G. Park, 2015 Symposium on VLSI Technology (VLSI Technology), IEEE, New York City, US, T120-T121, **2015**, 7223712, https://doi.org/10.1109/VLSIT.

© 2024 The Author(s). Advanced Materials Interfaces published by Wiley-VCH GmbH

21967350, 2025, 1, Downloaded from https://advanced.onlinelibrary.wiley.com/doi/10.1002/admi.202400558, Wiley Online Library on [06/05/2025]. See the Terms and Conditions (https://onlinelibrary.wiley.com/terms-and-conditions) on Wiley Online Library for rules of use; OA articles are governed by the applicable Creative Commons License

21967350, 2025, 1, Downloaded from https://advanced.onlinelibrary.wiley.com/doi/10.1002/admi.202400558, Wiley Online Library on [06/05/2025]. See the Terms and Conditions (https://onlinelibrary.wiley.com/terms-and-conditions) on Wiley Online Library for rules of use; OA articles are governed by the applicable Creative Commons License

[7] E. H. Sondheimer, *Adv. Phys.* **1952**, *1*, 1.
[8] A. F. Mayadas, M. Shatzkes, *Phys. Rev. B* **1970**, *1*, 1382.
[9] R. S. Smith, E. T. Ryan, C.-K. Hu, K. Motoyama, N. Lanzillo, D. Metzler, L. Jiang, J. Demarest, R. Quon, L. Gignac, C. Breslin, A. Giannetta, S. Wright, *AIP Adv.* **2019**, *9*, 025015.
[10] W. Steinhögl, G. Schindler, G. Steinlesberger, M. Traving, M. Engelhardt, *J. Appl. Phys.* **2005**, *97*, 023706.
[11] D. Gall, *J. Appl. Phys.* **2016**, *119*, 085101.
[12] D. Choi, *Nanosci. Nanotechnol. Lett.* **2018**, *10*, 1310.
[13] D. Gall, *J. Appl. Phys.* **2020**, *127*, 050901.
[14] D. Tierno, K. Croes, A. Ajaykumar, S. Ramesh, G. Van den Bosch, M. Rosmeulen, 2021 IEEE International Reliability Physics Symposium (IRPS) **2021**, 1, https://doi.org/10.1109/IRPS46558.9405132.
[15] V. Founta, J.-P. Soulié, K. Sankaran, K. Vanstreels, K. Opsomer, P. Morin, P. Lagrain, A. Franquet, D. Vanhaeren, T. Conard, J. Meersschaut, C. Detavernier, J. Van de Vondel, I. De Wolf, G. Pourtois, Z. Tőkei, J. Swerts, C. Adelmann, *Materialia* **2022**, *24*, 101511.
[16] I. Erofeev, A. W. Hartanto, K. Saidov, Z. Aabdin, A. Pacco, H. Philipsen, W. W. Tjiu, H. K. Hui, F. Holsteyns, U. Mirsaidov, *Adv. Electron. Mater.* **2024**, *10*, 2400035.
[17] D. Rafaja, H. Köstenbauer, U. Mühle, C. Löffler, G. Schreiber, M. Kathrein, J. Winkler, *Thin Solid Films* **2013**, *528*, 42.
[18] A. Pacco, Y. Akanishi, Q. T. Le, *Solid State Phenom.* **2021**, *314*, 295,.
[19] S. Decoster, E. Camerotto, G. Murdoch, S. Kundu, Q. T. Le, Z. Tőkei, G. Jurczak, F. Lazzarino, *J. Vac. Sci. Technol. B* **2022**, *40*, 032802.
[20] A. Jourdain, M. Stucchi, G. Van der Plas, G. Beyer, E. Beyne, 2022 IEEE 72nd Electronic Components and Technology Conf. (ECTC) 1531–1538. https://doi.org/10.1109/ECTC51906.2022.00244.
[21] S. S. T. Nibhanupudi, D. Prasad, S. Das, O. Zografos, A. Robinson, A. Gupta, A. Spessot, P. Debacker, D. Verkest, J. Ryckaert, G. Hellings, J. Myers, B. Cline, J. P. Kulkarni, *IEEE Trans. Electron Devices* **2022**, *69*, 4453.
[22] P. A. Gargini, *IEEE Electron Devices Mag.* **2023**, *1*, 32.
[23] A. Fischer, A. Routzahn, T. Lill, *Meet. Abstr.* **2020**, *MA2020-02*, 1380.
[24] V. A. Petrochenkov, I. G. Gorichev, V. V. Batrakov, A. D. Izotov, A. M. Kutepov, *Theor. Found. Chem. Eng.* **2004**, *38*, 386.
[25] A. Pacco, T. Nakano, A. Iwasaki, S. Iwahata, E. A. Sanchez, *2021 IEEE International Interconnect Technology Conference (IITC)* **2021**, 1, https://doi.org/10.1109/IITC51362.9537407.
[26] A. Pacco, T. Nakano, S. Iwahata, A. Iwasaki, E. A. Sanchez, *J. Vac. Sci. Technol. A* **2023**, *41*, 032601.
[27] Y. Lee, Y. Kim, J. Son, H. Chae, *Journal of Vacuum Science & Technology A* **2022**, *40*, 022602.
[28] Y. Kim, H. Kang, H. Ha, C. Kim, S. Cho, H. Chae, *Appl. Surf. Sci.* **2023**, *627*, 157309.
[29] K. Saidov, I. Erofeev, Z. Aabdin, A. Pacco, H. Philipsen, A. W. Hartanto, Y. Chen, H. Yan, W. W. Tjiu, F. Holsteyns, U. Mirsaidov, *Adv. Funct. Mater.* **2023**, *34*, 2310838.
[30] N. Cabrera, N. F. Mott, *Rep. Prog. Phys.* **1949**, *12*, 163.
[31] F. P. Fehlner, N. F. Mott, *Oxid. Met.* **1970**, *2*, 59.
[32] L. P. Ramírez, F. Bournel, J.-J. Gallet, L. Dudy, F. Rochet, *J. Phys. Chem. C* **2022**, *126*, 2517.
[33] C. R. Stilhano Vilas, Boas, J. M., Sturm, W. T. E., van den Beld, F., *Bijkerk, Materialia* **2021**, *20*, 101203.
[34] J.-G. Choi, L. T. Thompson, *Appl. Surf. Sci.* **1996**, *93*, 143.
[35] D. J. Morgan, *Surf. Interface Anal.* **2023**, *55*, 567.
[36] Z. Aabdin, T. Ghosh, A. Pacco, S. Raj,H. T. B. Do, K. Saidov, T. Weei, U. Anand, P. Král. Holsteyns, M. Bosman, U. Mirsaidov, *ACS Appl. Electron. Mater* **2022**, *4*, 5191.
[37] U. Anand, T. Ghosh, Z. Aabdin, S. Koneti, X. Xu, F. Holsteyns, U. Mirsaidov, *Proc. Natl. Acad. Sci. U.S.A* **2021**, *118*, 2108074118.
[38] Aanalyzer: a peak-fitting program for photoemission data, https://xpsoasis.org/aanalyzer_manual (accessed: September 2023).
[39] G. van Rossum, F. L. Drake, *Python 3 Reference Manual*, CreateSpace, California, US **2009**.
[40] J. Daintith, *A Dictionary of Physics*, Oxford University Press, Oxford **2009**.

© 2024 The Author(s). Advanced Materials Interfaces published by Wiley-VCH GmbH